Physics in Medicine & Biology

IPEM Institute of Physics and Engineering in Medicine

ACCEPTED MANUSCRIPT • OPEN ACCESS

3D model-based super-resolution motion-corrected cardiac T1 mapping

To cite this article before publication: Simone Hufnagel *et al* 2022 *Phys. Med. Biol.* in press https://doi.org/10.1088/1361-6560/ac9c40

Title: 3D model-based super-resolution motion-corrected cardiac T1 Mapping

Authors: Simone Hufnagel[1], Selma Metzner[1], Kirsten Miriam Kerkering[1], Christoph Stefan Aigner[1], Andreas Kofler[1], Jeanette-Schulz-Menger[2,3,4], Tobias Schaeffter[1,5,6], Christoph Kolbitsch[1]

[1]Physikalisch-Technische Bundesanstalt (PTB), Braunschweig and Berlin, Germany

[2]Charité Medical Faculty University Medicine, Berlin, Germany

[3]Working Group on Cardiovascular Magnetic Resonance, Experimental and Clinical Research Center (ECRC), Charité Humboldt University Berlin, DZHK partner site Berlin, Berlin, Germany

[4]Department of Cardiology and Nephrology, HELIOS Klinikum Berlin Buch, Berlin, Germany

[5]School of Biomedical Engineering and Imaging Sciences, King's College London, London, United Kingdom

[6]Department of Biomedical Engineering, Technical University of Berlin, Berlin, Germany

Correspondence address:
Simone Hufnagel
Physikalisch-Technische Bundesanstalt
Braunschweig and Berlin
Germany
simone.hufnagel@ptb.de

word count (body): ~4682
word count (abstract): 237

Keywords: super-resolution; T_1 mapping; model-based reconstruction; cardiovascular MR; myocardial tissue characterization

Abstract

Objective: To provide 3D high-resolution cardiac T1 maps using model-based super-resolution reconstruction (SRR).

Approach: Due to signal-to-noise ratio (SNR) limitations and the motion of the heart during imaging, often 2D T1 maps with only low through-plane resolution (i.e. slice thickness of 6 to 8 mm) can be obtained. Here, a model-based SRR approach is presented, which combines multiple stacks of 2D acquisitions with 6 to 8 mm slice thickness and generates 3D high-resolution T1 maps with a slice thickness of 1.5 to 2 mm. Every stack was acquired in a different breath hold (BH) and any misalignment between BH was corrected retrospectively. The novelty of the proposed approach is the BH correction and the application of model-based SRR on cardiac T1 Mapping. The proposed approach was evaluated in numerical simulations and phantom experiments and demonstrated in four healthy subjects.

Main results: Alignment of BH states was essential for SRR even in healthy volunteers. In simulations, respiratory motion could be estimated with an RMS error of 0.18 ± 0.28 mm. SRR improved the visualization of small structures. High accuracy and precision (average standard deviation of 69.62 ms) of the T1 values was ensured by SRR while the detectability of small structures increased by 40%.

Significance: The proposed SRR approach provided T1 maps with high in-plane and high through-plane resolution (1.3×1.3×1.5 to 2 mm^3). The approach led to improvements in the visualization of small structures and precise T1 values.

Introduction

Cardiovascular MR is a well-established technique for the diagnosis of cardiac diseases. Over the last years, T1 mapping has been translated into clinical application as an important quantitative approach for cardiac tissue differentiation[1]. It has been demonstrated that T1 mapping can be used to diagnose a wide range of different cardiac pathologies, including entities with preserved ejection fraction[2–4].

However, one of the major challenges in cardiac T1 mapping is that the achievable image resolution is often restricted due to respiratory and cardiac motion, SNR and limited acquisition time. In clinical practice, T1 maps are acquired with a 2D acquisition scheme resulting in one slice per breath hold (BH) that has a high in-plane resolution but suffers from a poor through-plane resolution of 6-8 mm[5]. 3D T1 Mapping has been proposed but with a long acquisition time[6,7]. With the work proposed in [8], 80% of the cardiac cycle can be used for T1 mapping, allowing the acquisition of six slices with a slice thickness of 6-8 mm per BH. Nonetheless, image resolution is compromised by partial volume effects. This can impair the accurate detection of subtle fibrosis in the myocardium in different entities and limit the capability to differentiate myocardial injury within the thin myocardial wall of young patients.

Super-resolution reconstruction (SRR) has been proposed to improve the tradeoff between spatial resolution, acquisition time and SNR[9-19]. The resolution is thereby increased by acquiring various low-resolution (LR) images with complementary information about the object. This is ensured by shifting the image positions of the LR stacks along the slice direction or by changing their slice orientations. Subsequently, the LR stacks are combined into a high-resolution (HR) data set by solving an inverse problem. The reconstructed HR image thus benefits from the high SNR of the LR images while providing HR diagnostic information. For quantitative MRI, the parametric model of the mapping can be combined with the SRR model which has been demonstrated on the brain[20,21]. Such a model-based SRR enables the direct estimation of HR T1 maps from LR T1-weighted images (dynamics).

The principle of SRR is based on knowledge about the geometric relationship between different LR datasets. Motion leads to misalignment and strongly impairs the achievable image quality of SRR[22]. The application of SRR on the heart[23–31] has so far only been shown for qualitative imaging. For T1 Mapping, SRR taking into account different motion states of the individual LR stacks has so far only been applied on the brain[20,32,33] .

The application of SRR to quantitative cardiac MRI data is especially challenging due to cardiac and respiratory motion. Next to that, the acquisition during breath hold imposes severe limitations on the acquisition time and thus limits the number of slices per LR stack. So far, no model-based SRR T1 mapping has been applied on cardiac data, which requires advanced acquisition and motion correction (moco) schemes.

In this study, we present a model-based SRR for cardiac T1 mapping, providing precise HR T1 maps with improved visualization of small structures compared to the direct LR acquisitions. It combined multiple stacks of 2D acquisitions with 6 to 8 mm slice thickness and generated 3D HR T1 maps with a target slice thickness of 1.5 to 2 mm in six to ten BH. Cardiac and residual respiratory motion was corrected. The approach was evaluated in native T1 mapping in numerical simulations and phantom experiments and feasibility was demonstrated in four healthy volunteers.

Methods

The proposed workflow to achieve motion-corrected model-based SRR T1 maps is depicted in Figure 1: Multiple stacks of 2D slices were acquired continuously with one stack per BH. In a first step, non-rigid cardiac motion was estimated and used in a model-based T1 reconstruction[5] resulting in the dynamics γ^{w} and parameter maps γ^{m} (6 slices à 6 to 8mm per stack) which are all in the same cardiac motion state. In a second step, the stacks were registered to each other to estimate and compensate for different BH positions. After the motion alignment, the maps were then used to calculate the first estimate of the HR map Γ_{0}^{m} as initialization of the SRR. Finally, a HR T1 map Γ_{final}^{m} was generated by SRR.

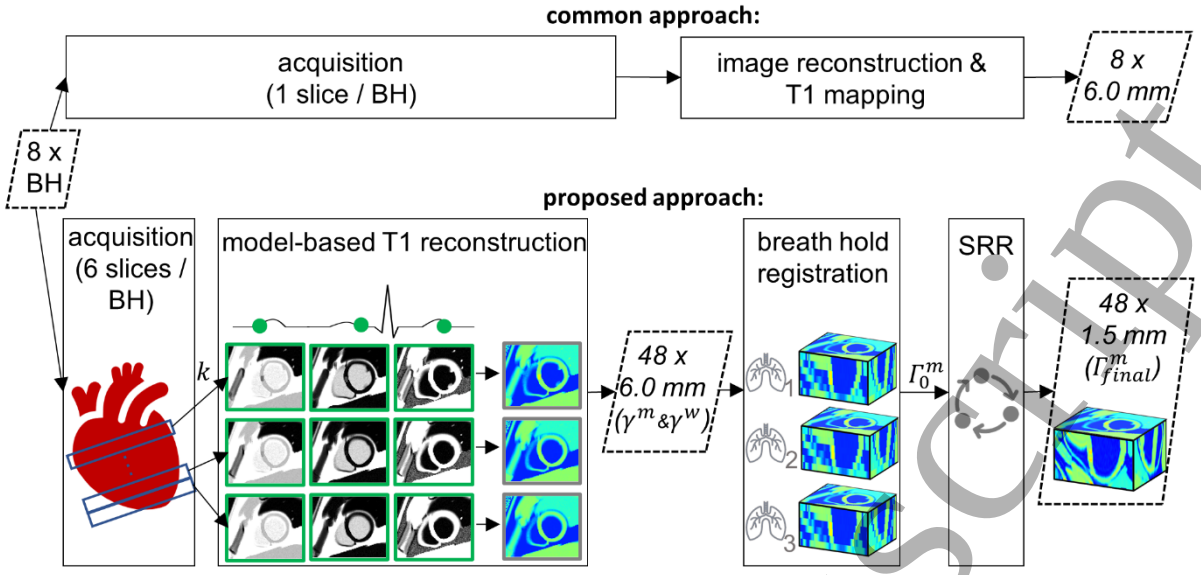

Figure 1: Comparison of the proposed motion-corrected model-based SRR workflow and the common approach. In this schematic comparison, data was acquired over eight breath holds (BH). In the common approach, one slice could be reconstructed per BH. In the proposed approach, one stack per BH with six 2D slices each was acquired. Cardiac motion was estimated and included in a model-based T1 reconstruction of the k-space data k yielding the dynamics γ^w and the parameter maps γ^m of the LR stacks. Then, the different stacks were registered to each other. The motion corrected γ^m were used to calculate the first estimate of the HR map Γ_0^m and SRR yielded the final 3D HR parameter map Γ_{final}^m. In this example, the proposed approach led to six times more slices with the same number of BH, with a slice thickness reduced by a factor of four compared to the common approach.

Data acquisition

Data was acquired using a Golden-angle radial sampling scheme on 3 Tesla MR scanner (Verio, Siemens Healthineers, Erlangen, Germany) with a commercial 32-channel cardiac coil. After a slice-selective radio-frequency inversion pulse, data was continuously acquired in multiple stacks with six slices each resulting in an acquisition time of 16.8s for a single stack (2.8s for each slice) with the following parameters: flip angle α=5°, resolution 1.3×1.3×6.0 to 8.0 mm³, FOV 320×320×84 to 105 mm³, TE/TR: 2.19/4.9 ms, orientation short-axis-view, subject specific slice gap of 4 to 9 mm to cover the desired FOV while avoiding slice interference from the radio-frequency inversion and excitation radio-frequency pulses. Six to ten stacks (one stack per BH) were acquired in total with an offset of 1.5 to 2 mm between stacks along the slice direction. Due to the short acquisition time, a slice-selective inversion pulse was used in combination with an interleaved multi-slice ordering. The ECG was recorded for retrospective cardiac moco.

Model-based T1 reconstruction

Dynamic cardiac motion-resolved images were reconstructed with a temporal resolution of 44.1 ms. Spatial and temporal total variation regularization (regularization parameters λ along time and space were 0.5) was applied to suppress undersampling artefacts[34]. To accelerate the motion estimation, a subject specific rectangular region of interest covering both ventricles was selected. In an iterative fashion, the non-rigid cardiac motion was estimated using the MIRTK Toolkit[35].

The estimated cardiac motion information was used in an iterative model-based T1 reconstruction[5,8]. Data from the entire cardiac cycle was used, except for the 30% of the systole with the greatest through-plane motion. A Look-Locker model q was used in an iterative reconstruction scheme to estimate γ^{m} with the quantitative parameter $\mathrm{m} = [\mathrm{p}, \alpha, \mathrm{T1}]$ and γ^{w} with a temporal resolution of 83.3 ms, p denoting the equilibrium magnetization and α the flip angle. In the following, only the T1 parameter is mainly considered because it is clinically the most relevant.

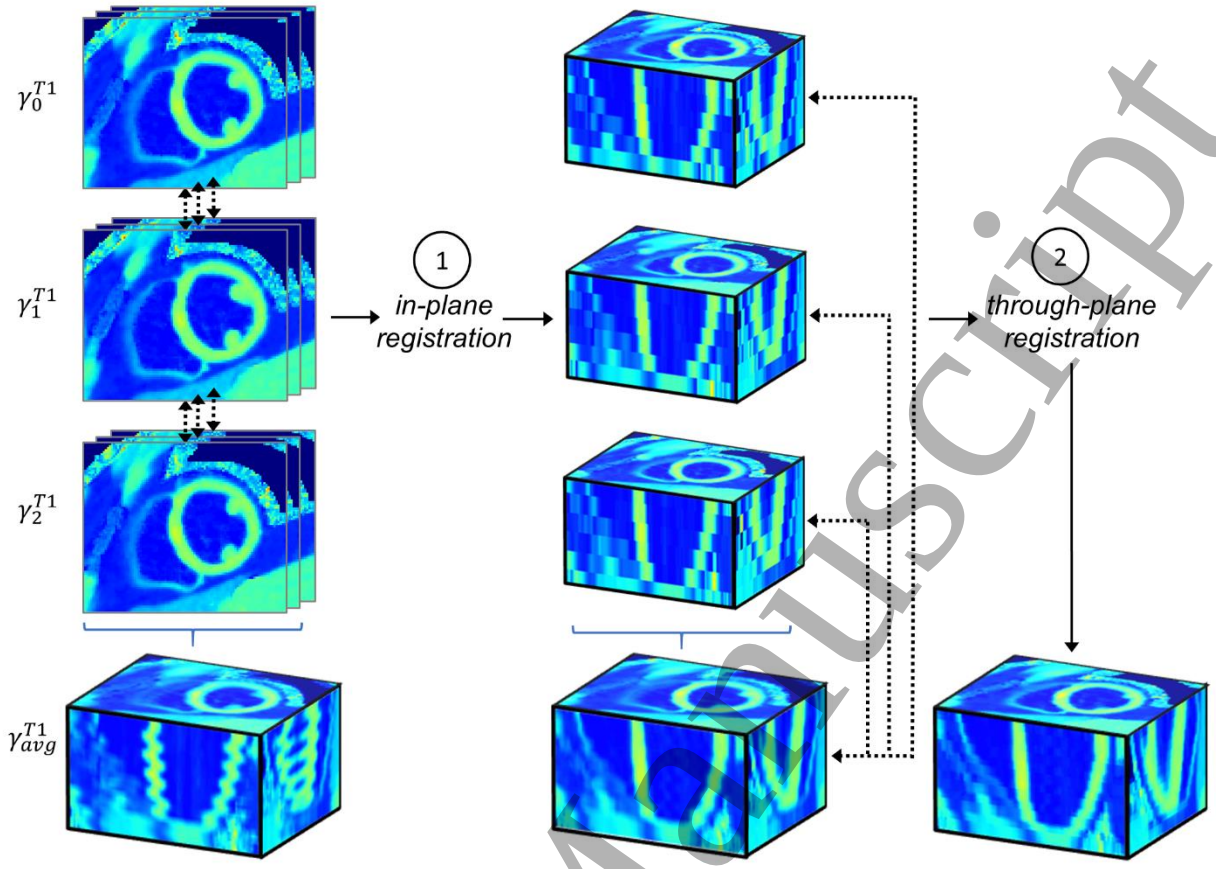

Figure 2: Breath hold registration scheme. Different breath hold positions of the uncorrected T1 maps of the individual LR stacks, three of which are shown as an example ($\gamma_0^{T1}, \gamma_1^{T1}, \gamma_2^{T1}$), led to artifacts when combining them in γ_{avg}^{T1}. In the first step, each LR slice was registered to the closest slice in the neighboring stack (in-plane registration), leading to a reduction of artifacts in the orthogonal view of γ_{avg}^{T1}. In the subsequent through-plane registration, each LR stack was registered to γ_{avg}^{T1} in an iterative fashion.

Each stack was acquired in a different BH. To correct for potential misalignments of BH positions, the stacks were registered to each other using a cross-correlation approach[36]. A two-stage process was developed for this purpose (Figure 2). In the first step of the motion estimation, the rigid motion in the in-plane direction of the slices γ_s^m was determined. For that, the T1 maps of the LR slices of stacks s were registered to each other: Each slice of each stack was registered to the slice which was closest (i.e. smallest distance along the slice direction) to it. The stacks were acquired in an overlapping fashion, therefore the closest slice was part of another stack and hence, γ_s^{T1} was registered to $\gamma_{(s-1)}^{T1}$ using a phase-cross-correlation registration. That yielded information about the in-plane motion of every slice of

every stack. The median of the motion detected in its six slices was finally assigned to the entire stack of LR slices .

In the second step, the LR stacks were registered with respect to shifts along the slice encoding direction. For that, γ_s^{T1} was interpolated along the slice encoding direction using bicubic spline interpolation, which also filled the gaps between the LR slices. The interpolated T1 maps of the LR stacks were then combined and an average stack γ_{avg}^{T1} was calculated. In an iterative process, each stack was then registered to γ_{avg}^{T1}. In the next iteration a new γ_{avg}^{T1} was calculated taking the estimated motion into account. Only translational shifts were considered. Two iterations were used in total.

Model-based super-resolution reconstruction

For SRR, several LR stacks acquired with an offset to each other were combined to an HR volume. The model q calculates dynamics from given parameter maps. The SRR used here is model-based and thus q was incorporated into SRR to at the end obtain a HR T1 map Γ^m from γ^w. As initialization Γ_0^m of the SRR, γ^m were calculated from γ^w using a voxel-wise 3-parameter T1 fit and combined:

$$\Gamma_{0,h}^m = \sum_{s=1}^{S}\sum_{l=1}^{L} a_s^{h,l}\gamma_{s,l}^m \tag{1}$$

In order to describe the effect of the excitation slice profile, a resolution model was calculated from Bloch simulations of the RF pulse[37,38]. The slice profile simulations were used to describe the weight $a_s^{h,l}$ of HR slice h with respect to LR slice l in stack s (with $h = 1,\dots,H$, $l = 1,\dots,L$ and $s = 1,\dots,S$ and H, L, and S being the number of HR-slices, the number of LR-slices and the number of stacks, respectively). With that, LR dynamics $\widetilde{\gamma_{t,s,l}^w}$ (with $t = 1,\dots,T$, and T being the number of inversion times) were calculated:

$$\widetilde{\gamma_{t,s,l}^w}(\Gamma^m) = \sum_{h=1}^{H} a_s^{h,l} q_t(\Gamma_h^m) \tag{2}$$

A functional based on the sum of the differences between the LR slices and stacks of the predicted ($\widetilde{\gamma_{t,s,l}^w}$) and acquired LR dynamics ($\gamma_{t,s,l}^w$) and a total variation based regularization term was minimized, which could be described by the following minimization problem:

$$\min_{\Gamma^m} \sum_{t=1}^{T}\sum_{s=1}^{S}\sum_{l=1}^{L} \left|\left|\gamma_{t,s,l}^w - \widetilde{\gamma_{t,s,l}^w}(\Gamma^m)\right|\right|_2^2 + \kappa \left|\left|G\Gamma^m\right|\right|_1 \tag{3}$$

where κ describes the regularization parameter and G corresponds to the forward finite differences operator. As $a_s^{h,l}$ describes the relationship between a HR and LR slice, by solving Problem (3) an estimate of the HR slices could be recovered. Since solving problem (3) directly is challenging due to the non-smoothness of the L1-norm as well as the non-linear function q, a variable splitting[21,39] approach was used. This allowed solving the resulting sub-problems with suitable algorithms. By introducing auxiliary variables $x_t := q_t(\Gamma^m)$ for all t and $u := \Gamma^m$ the problem was reformulated as a joint minimization problem. These equalities were relaxed by including two quadratic penalty terms, weighted by λ and μ, yielding:

$$\min_{\Gamma^m,\ x,\ u} \sum_{t=1}^{T}\sum_{s=1}^{S}\sum_{l=1}^{L}\left\|\gamma_{t,s,l}^{w} - \sum_{h=1}^{H} a_s^{h,l}\, x_{t,h}\right\|_2^2 + \lambda\left||x_t - q_t(\Gamma^m)|\right|_2^2 + \mu\left||u - \Gamma^m|\right|_2^2 + \kappa\left||Gu|\right|_1 \tag{4}$$

The solution of problem (4) was approached by alternating the minimization of (4) with respect to one of the variables and keeping the other two fixed. For fixed Γ^m, u, updating x corresponded to solving

$$\min_{x} \sum_{t=1}^{T}\sum_{s=1}^{S}\sum_{l=1}^{L}\left\|\gamma_{t,s,l}^{w} - \sum_{h=1}^{H} a_s^{h,l}\, x_{t,h}\right\|_2^2 + \lambda\left||x_t - q_t(\Gamma^m)|\right|_2^2 \tag{Sub1}$$

Subproblem (Sub1) was minimized with respect to x, assuming Γ^m and u are fixed. Solving (Sub1) involved solving a linear system for which a conjugate gradient approach was used.

For fixed Γ^m, x, updating u in problem (4) corresponded to solving

$$\min_{u} \mu/\kappa\left||u - \Gamma^m|\right|_2^2 + \left||Gu|\right|_1 \tag{Sub2}$$

Subproblem (Sub2) was solved using the iterative algorithm proposed in [40].

For fixed u and x, updating Γ^m in problem (4) corresponded to solving

$$\min_{\Gamma^m} \sum_{t=1}^{T} \lambda\left||x_t - q_t(\Gamma^m)|\right|_2^2 + \mu\left||u - \Gamma^m|\right|_2^2 \tag{Sub3}$$

Due to the non-linearity of function q, the Limited-memory Broyden–Fletcher–Goldfarb–Shanno algorithm[41] was used for solving problem (Sub3). To solve problem (4), the subproblems were alternated eight times and the solution of problem (3) was referred to as Γ_{final}^m.

Simulation experiments

Simulated data was generated using the XCAT phantom[42]. A dataset X_{orig} with the voxel size 1.3x1.3x0.5 mm was generated. From this, eight stacks of LR dynamics were simulated with the same parameters used for the phantom and the in vivo experiments (slice thickness of 6 mm, a gap between the LR slices of 6 mm and an offset between the stacks of 1.5 mm). As reference X_{ref}, a dataset with a slice thickness of 1.5 mm was generated from X_{orig}. In X_{orig}, two cubical fibrotic structures were simulated in the septum with a width of 6 mm each along the slice encoding direction. They were separated by a 6 mm gap of healthy myocardium. Cardiac motion was simulated using the default settings of the XCAT phantom. Data acquisition was simulated with multiple receiver coils using the same acquisition parameters as for the phantom and the in vivo experiments. Zero-mean noise was added. This allowed the application of the entire pipeline including model-based T1 reconstruction and cardiac moco on the simulated data.

In the simulations, a T1 time of 1300 ms was assigned to the myocardium, 400 ms to fat, 800 ms to the liver, 900 ms to muscle and 1800 ms to the simulated fibrosis. Blood was simulated with an apparent T1 time of 350 ms, as it could not be estimated due to the in-flow effect caused by the slice-selective inversion pulse[43].

Two different types of simulations were carried out. First, a simulation assuming perfect BH (i.e. no misalignment between different BH) was performed to evaluate the possible improvement that could be achieved with SRR. In a second step, misalignment between the BH was included into the simulation. Different BH positions were simulated by applying translation shifts. 20 configurations with different breath-hold positions of the stacks were simulated. The simulated motion was in the range of (3.5, 1.9, 8.2) mm in the (anterior-posterior, right-left, food-head) direction, based on half of the motion range between end expiration and end inspiration measured in [44]. For reasons of computational time, no heart motion was included in this simulation.

To assess the outcome of the SRR applied on simulated data, the detectability d between the simulated fibrosis and surrounding healthy myocardium was measured, using the following formula:

$$d = (\mu_{structure} - \mu_{nextStructure}) / \sigma_{background} \quad (5)$$

Where the mean T1 value $\mu_{structure}$ was measured in a region-of-interest (ROI) within the fibrosis, the mean T1 value $\mu_{nextStructure}$ was calculated in a ROI next to the fibrosis and the standard deviation (SD) $\sigma_{background}$ was calculated from a ROI in the surrounding healthy myocardium. The ROI was calculated from the position of the simulated fibrotic structures in X_{orig}.

To evaluate the breathing moco, the RMS error ϵ between the originally simulated motion and the estimated motion was calculated in mm.

The LR data in the proposed approach was always acquired in the same orientation according to the short-axis-view of the heart. To assess through-plane resolution, images in this publication are often presented orthogonally from the side, resulting in a four-chamber view.

Phantom experiments

To evaluate the proposed approach in phantom measurements, imaging was performed with the above-described scan parameter in a "T1MES-phantom" with nine tubes with different T1 times developed for cardiac imaging[45]. In order to cover the whole phantom with every stack, 12 slices per stack were acquired. Furthermore, a scan $\gamma^{\mathrm{m}}_{\mathrm{orth}}$ orthogonal to the LR data was acquired, where the slice encoding direction of γ^{m} became an in-plane direction of $\gamma^{\mathrm{m}}_{\mathrm{orth}}$. As a reference, an inversion recovery spin-echo $\mathrm{ref}_{\mathrm{SE}}$ was acquired, also in orthogonal direction to the LR data with 7 TIs between 25 and 4800 ms (TE/TR: 12/8000 ms, FOV: 143 × 160 mm^2, spatial resolution: 0.8 × 0.8 × 5 mm^3).

To assess the outcome of the SRR applied on the T1MES phantom, a ROI was drawn in every tube in γ^{m}, Γ^{m}_{0}, $\Gamma^{\mathrm{m}}_{\mathrm{final}}$ and $\mathrm{ref}_{\mathrm{SE}}$. The mean and SD of the T1 values were compared to assess T1 accuracy and precision, respectively. The Pearson's correlation coefficient and the two-tailed P-value between γ^{m}, Γ^{m}_{0}, $\Gamma^{\mathrm{m}}_{\mathrm{final}}$ and $\mathrm{ref}_{\mathrm{SE}}$ were calculated.

To evaluate the outcome of the BH moco, another dataset was acquired with phantom data at different, well-defined positions simulating different BH positions. The different positions were in the range (5.0, 2.4, 5.0) mm compared to the reference position. The reference motion was known for this acquisition and the Root-Mean-Squared Error (RMSE) to the estimated motion was calculated.

In vivo experiments

To evaluate the proposed approach in in vivo measurements, data was obtained from four healthy subjects (4 males, aged 34.0 ± 11.7 y). All subjects gave written informed consent before participation, in accordance with the institution's ethical committee. For the in vivo data, an orthogonal scan $\gamma^{\mathrm{m}}_{\mathrm{orth}}$ was acquired.

For reference, a 3(3)3(3)5 modified Look-Locker inversion recovery (MOLLI) scan Γ^{MOLLI} was acquired with the following scan parameter: FOV: 360 × 306 mm^2, TE/TR: 1.12/2.7 ms, flip angle: 35°, and spatial resolution: 2.1 × 1.4 × 6 mm^3 once in four chamber (4CH) and once in two chamber (2CH) orientation. The T1 values of the SRR result and MOLLI reference were compared using a ROI placed in the septum.

To assess the outcome of the SRR applied on in vivo data, $\gamma^{\mathrm{m}}_{\mathrm{orth}}$ was qualitatively compared to $\Gamma^{\mathrm{m}}_{\mathrm{final}}$. The precision of the T1 values was evaluated quantitatively by comparing the bull's eye plots[46] before and after the SRR, using four selected slices (apex, apical, mid-cavity and basal) and calculating the SD over four healthy volunteers. No fibrotic tissue was present in the healthy volunteers and therefore the detectability of the right ventricle was calculated to assess the effect of SRR on small structures.

The edge sharpness of the left ventricle in the anterior apical segment of the ventricle was calculated for γ^{m}, Γ^{m}_{0} and $\Gamma^{\mathrm{m}}_{\mathrm{final}}$. Edge sharpness was calculated by manually drawing a line along the edge of interest, gathering the intensities perpendicular to the line, and generating an average edge profile. The first-order derivative of the edge profile was calculated and edge sharpness of 100% referred to the case when the maximum derivative of the average edge profile was equal to the maximum intensity difference in the average edge profile, similar to [47].

Results

Simulation experiments

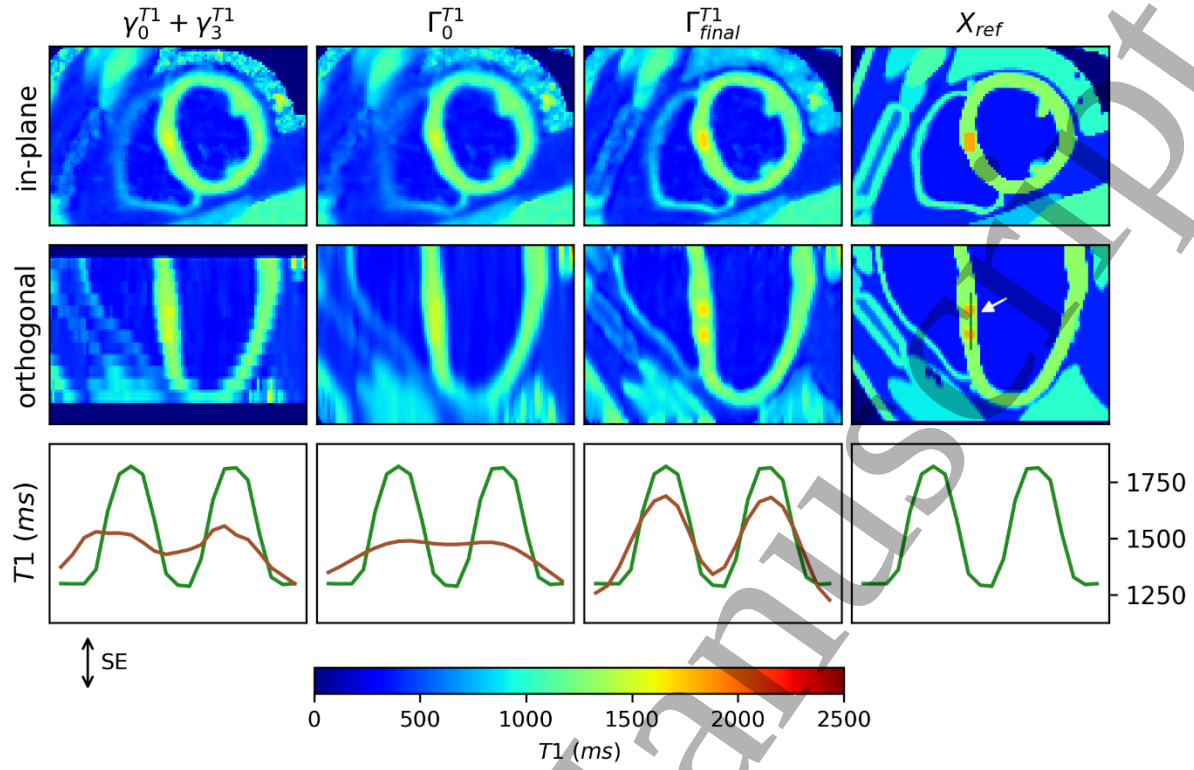

Figure 3: Results of the numerical simulation. The combination of the LR stacks γ_0^{T1} and γ_3^{T1}, the SRR initialization Γ_0^{T1} and the SRR output Γ_{final}^{T1} are shown and compared to the reference X_{ref}.Cardiac motion was simulated and corrected. No different breath hold states were simulated. The line plot shows the T1 values in the septum in slice encoding direction (SE) in brown along the line (white arrow) shown in X_{ref}, compared to the reference values in green. The distinction between pathological and healthy tissue was improved by SRR. The SRR improved the visualization of the apex compared to Γ_0^{T1}.

Figure 3 shows the results of the numerical simulations assuming perfect BH positions. In the LR stacks the two different fibrotic structures could not be distinguished along the slice encoding direction. The apex was inaccurately depicted in Γ_0^{T1}. Its visualization improved after SRR. d of the fibrosis increased from 0.03 in Γ_0^{T1} to 4.38 in Γ_{final}^{T1}.

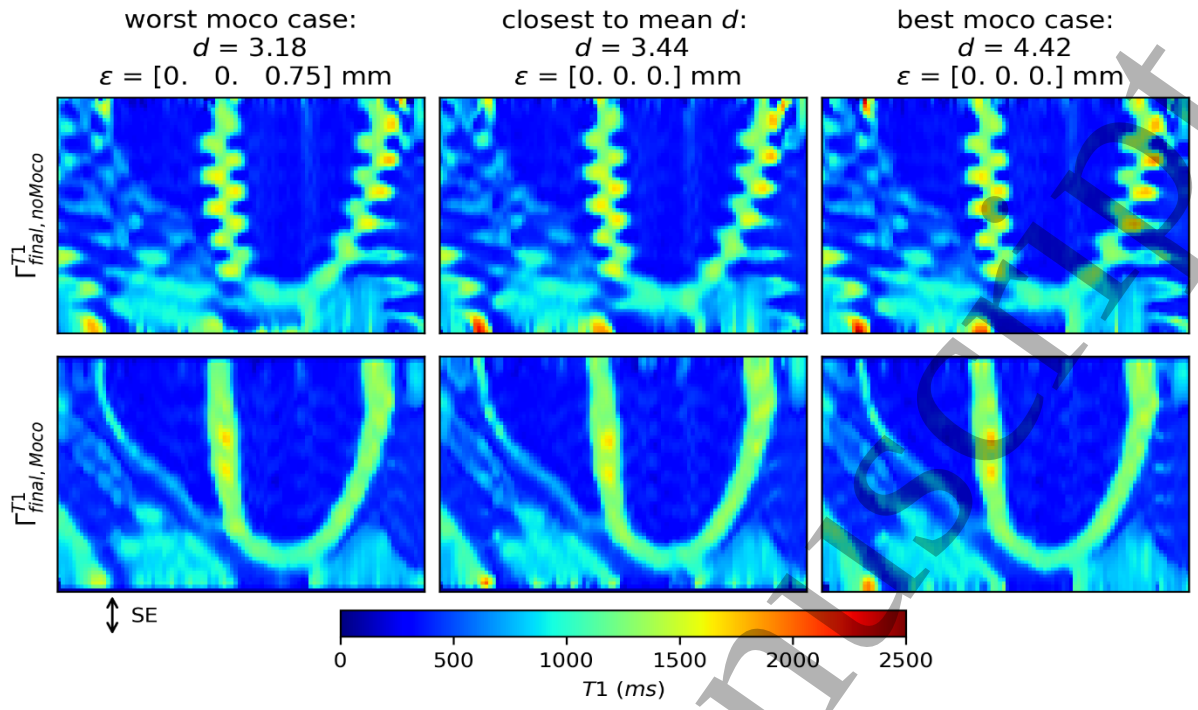

Figure 4: SRR applied to simulated data with stack specific breath hold states. The best and worst result of the motion correction (moco) out of 20 simulations is shown, measured by the moco error in mm (ε). In the middle column, the simulation with the detectability d closest to the mean d is shown. The result of SRR without moco ($\Gamma^{T1}_{final,noMoco}$) is compared to the result including moco ($\Gamma^{T1}_{final,Moco}$). SE indicates slice encoding direction.

Figure 4 shows the SRR applied on simulated data, simulated with different BH positions for every stack. $\Gamma^{\mathrm{T1}}_{\mathrm{final}}$ is shown without moco ($\Gamma^{\mathrm{T1}}_{\mathrm{final,noMoco}}$) and with applying the calculated motion ($\Gamma^{\mathrm{T1}}_{\mathrm{final,Moco}}$), once from the simulation with ϵ = 0 (best case),with the largest ϵ (worst case) and once for the simulation with a d closest to the mean d of all simulationsMoco improved the outcome of the SRR. In the best moco case, the differentiation of healthy and pathological tissue was more clear compared to the worst moco case. d of the simulated fibrosis over all 20 simulations after applying the calculated motion was 3.55 ± 0.54 in $\Gamma^{\mathrm{T1}}_{\mathrm{final,Moco}}$. d after applying the correct motion was 3.62 ± 0.5. d in $\Gamma^{\mathrm{T1}}_{\mathrm{final,noMoco}}$ was not calculated, because the fibrosis could not be detected for these T1 maps, as Figure 4 shows. The error ϵ over all simulations was (0.0, 0.0, 0.18) ± (0.0, 0.0, 0.28) mm.

Phantom experiments

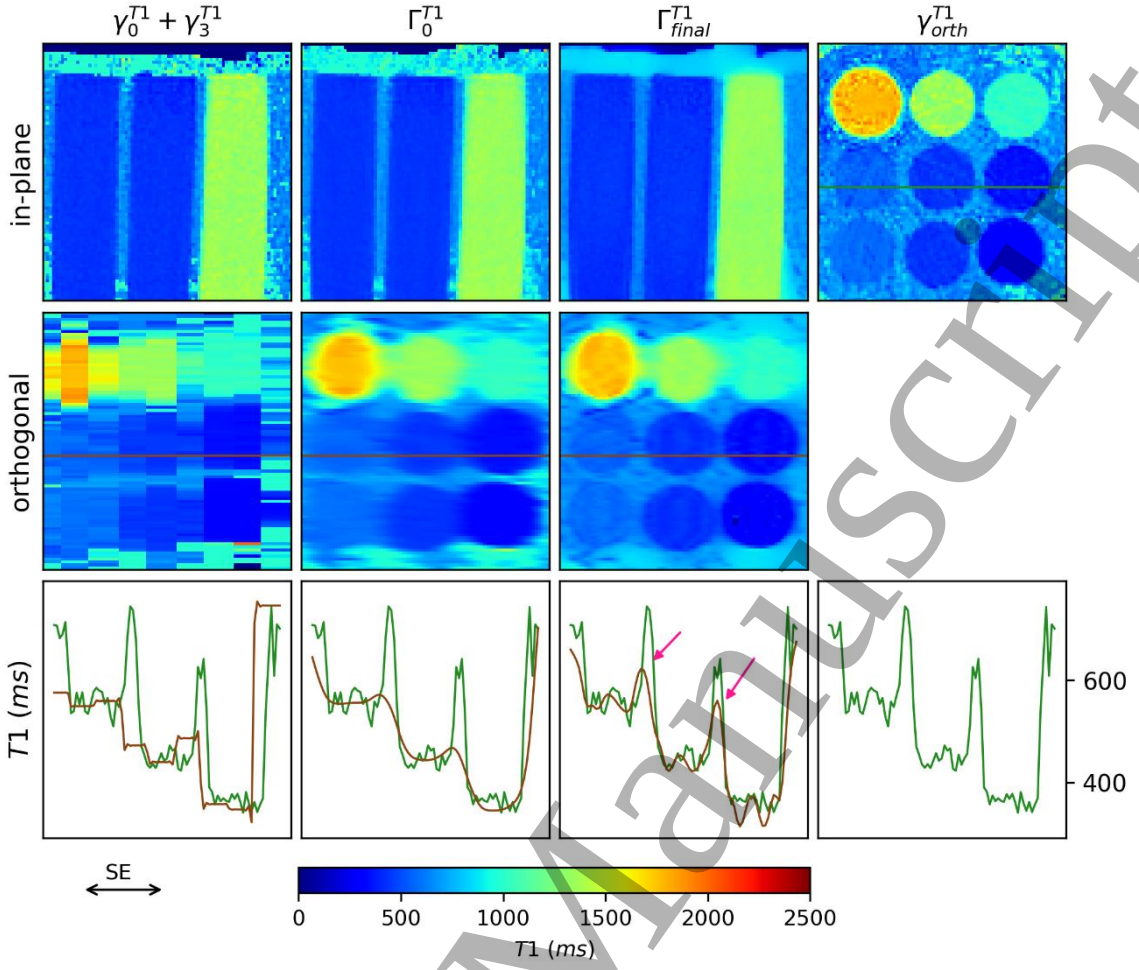

Figure 5: SRR applied on phantom data. The in-plane view and the orthogonal reformation of the combination of the LR stacks γ_0^{T1} and γ_3^{T1}, the SRR initialization Γ_0^{T1} and its output Γ_{final}^{T1} is compared with an orthogonal acquisition γ_{orth}^{T1}. A line plot through three tubes (brown line) along the slice encoding direction (SE) shows an improved differentiation (pink arrows) between tubes and background after SRR as shown by the reference in green.

Figure 5 shows the in-plane view and the orthogonal reformation of γ^{T1}, Γ_0^{T1} and Γ_{final}^{T1} and compares it to an orthogonal acquisition γ_{orth}^{T1}. A line plot through three tubes along the slice encoding direction shows an improved differentiation between tubes and background after SRR.

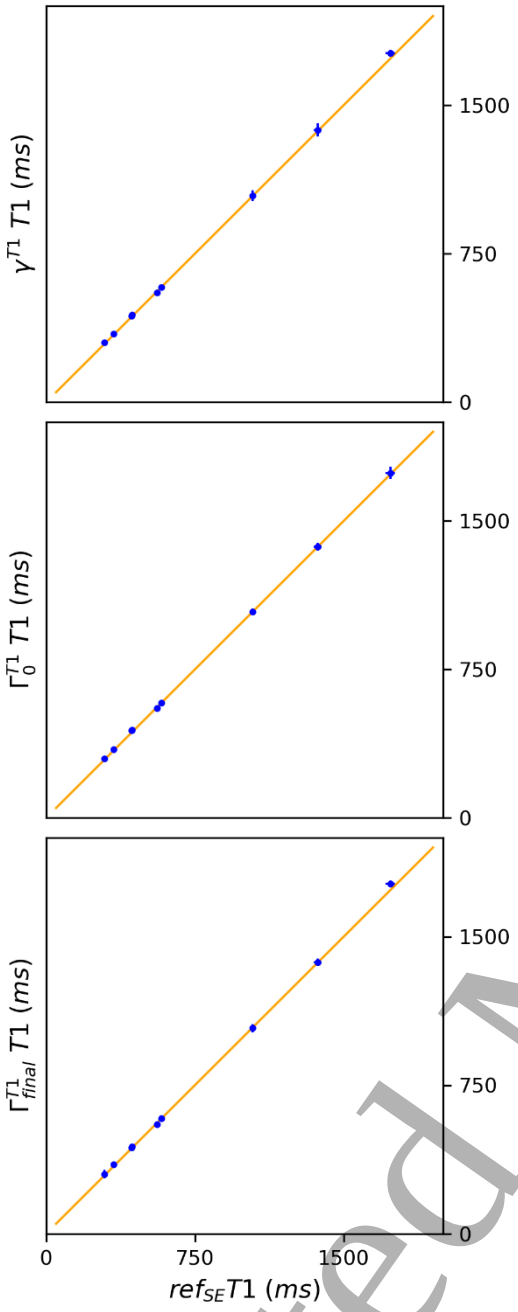

Figure 6: T1 values obtained with an inversion recovery spin-echo reference ref_{SE} scan are compared to the combination of LR stacks γ^{T1}, the initialization of SRR Γ_0^{T1} and the final SRR result Γ_{final}^{T1}.

Figure 6 assesses the accuracy of SRR: γ^{T1}, Γ_0^{T1} and Γ_{final}^{T1} showed high correlation with the reference scan ($P<0.001$, $R^2>0.999$). The mean difference between the T1 values of ref_{SE} and Γ_{final}^{T1} was 7.65 ± 9.24 ms. The difference of γ^{T1} and Γ_0^{T1} to ref_{SE} was 7.74 ± 7.09 ms and 5.41 ± 3.7 ms, respectively, indicating high accuracy of the SRR.

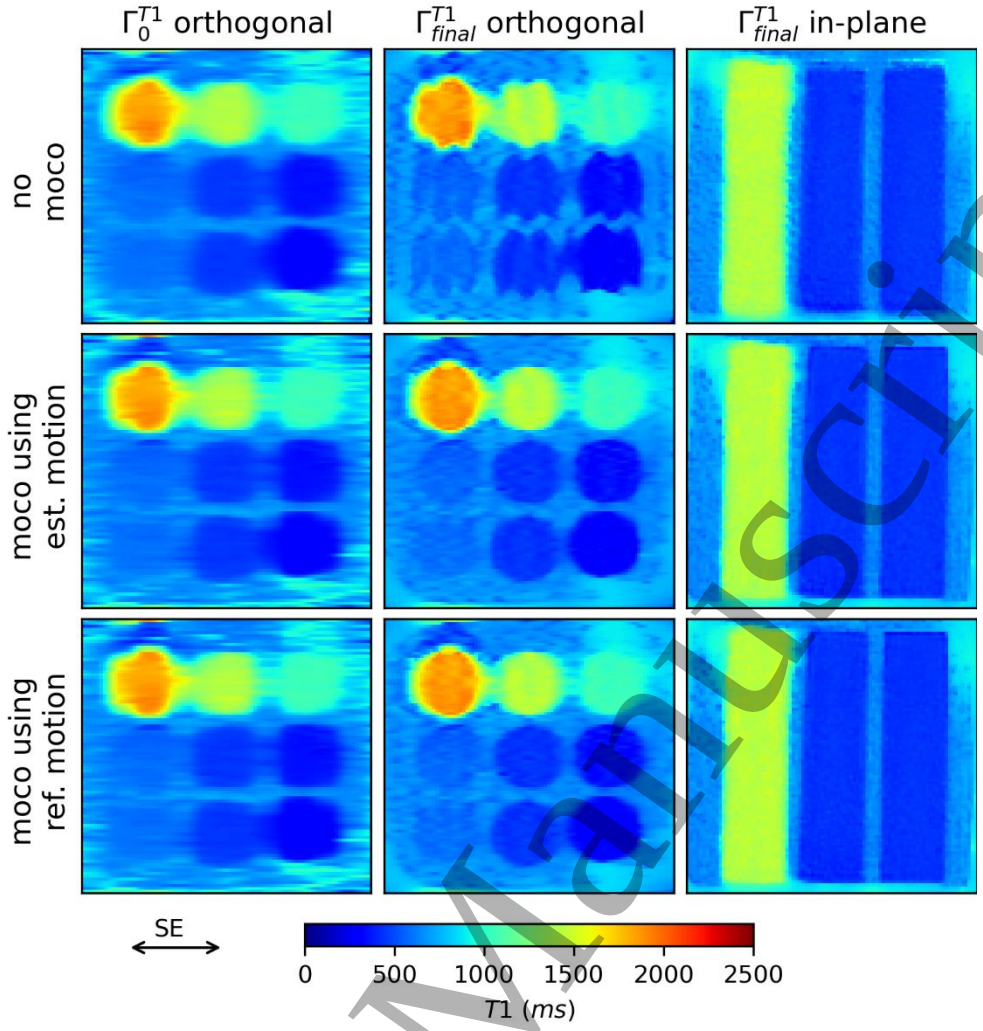

Figure 7: Simulated motion in the phantom experiment. The orthogonal view of the SRR initialization Γ_0^{T1}, the final SRR output Γ_{final}^{T1} as well as the in-plane view of Γ_{final}^{T1} are shown when no motion correction (moco) was performed, when the estimated (est.) motion was applied and when the reference (ref.) motion was used during moco. SE indicates the slice encoding direction.

Figure 7 shows the application of SRR on phantom data acquired at different positions simulating different BH positions. The orthogonal view of Γ_0^{T1} and Γ_{final}^{T1} and the in-plane view of Γ_{final}^{T1} are shown without moco, when the estimated motion was applied and when the reference motion was applied during moco. SRR without moco shows motion artefacts, which could be removed after applying the calculated moco. The visual result after applying the estimated motion shifts is similar to applying the reference motion shifts during moco. The RMSE between estimated and reference motion was (0.03, 0.04, 0.61) mm.

In vivo experiments

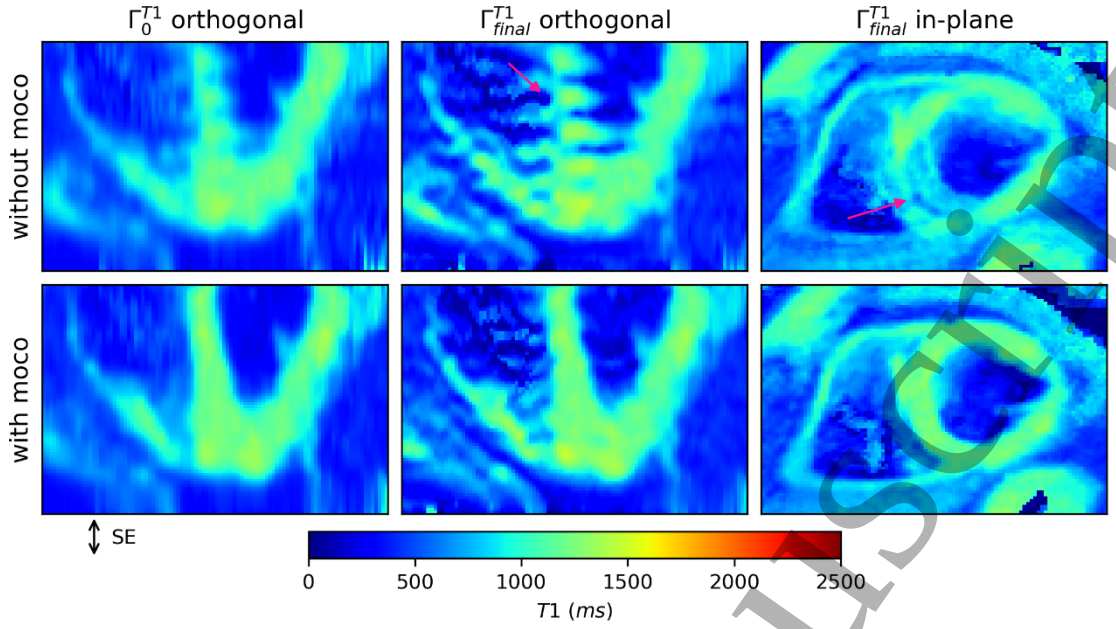

Figure 8: Impact of respiratory motion correction (moco) on in-vivo data. The orthogonal view of the SRR initialization Γ_0^{T1}, the final SRR output Γ_{final}^{T1} as well as the in-plane view of Γ_{final}^{T1} are shown without and with moco.

Figure 8 compares the orthogonal view of Γ_0^{T1} and Γ_{final}^{T1} and the in-plane view of Γ_{final}^{T1} with and without moco. Without BH alignment, motion artefacts could be seen in the form of a discontinuous septum in the orthogonal view and an ambiguous delineation of the myocardium in the in-plane view, which is highlighted by the pink arrows in the figure. The motion artefacts were less visible in the initialization of the SRR compared to its output. Using the proposed BH registration and subsequent correction, the motion artefacts after SRR could be reduced.

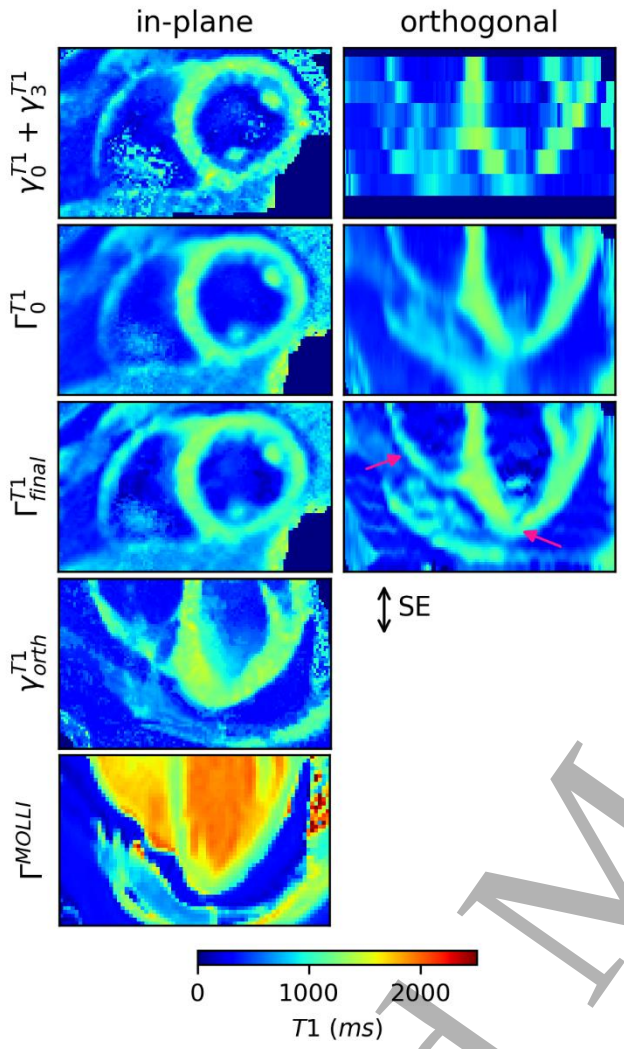

Figure 9: SRR applied on in vivo data. The combination of the LR stacks γ_0^{T1} and γ_3^{T1}, the SRR initialization Γ_0^{T1} and the SRR output Γ_{final}^{T1} are reformatted orthogonally and compared to a direct orthogonal acquisition γ_{orth}^{T1} and to a MOLLI reference scan Γ^{MOLLI}. All the results shown were obtained with the proposed moco approach. The visualization of the apex and the right ventricle improved after SRR (pink arrows). Due to the slice-selective inversion pulse, blood appeared with a low T1 value. SE indicates slice encoding direction.

Figure 9 shows the in-plane view and the orthogonal reformation of γ^{T1}, Γ_0^{T1}, $\Gamma_{\mathrm{final}}^{\mathrm{T1}}$ and compares it to an orthogonal acquisition $\gamma_{\mathrm{orth}}^{\mathrm{T1}}$ and Γ^{MOLLI}. Due to the slice-selective inversion pulse, blood appeared with a low T1 value. The visualization of the apex as well as the differentiation between the right ventricle and blood improved after SRR. Due to scan time limitations, $\gamma_{\mathrm{orth}}^{\mathrm{T1}}$ could not be acquired for one volunteer. The mean T1 value across all volunteers in a ROI in the septum in $\Gamma_{\mathrm{final}}^{\mathrm{T1}}$ was 1.21 ± 0.08 and in Γ^{MOLLI} 1.28 ± 0.04. One volunteer had to be excluded from the calculation because no MOLLI scan was available.

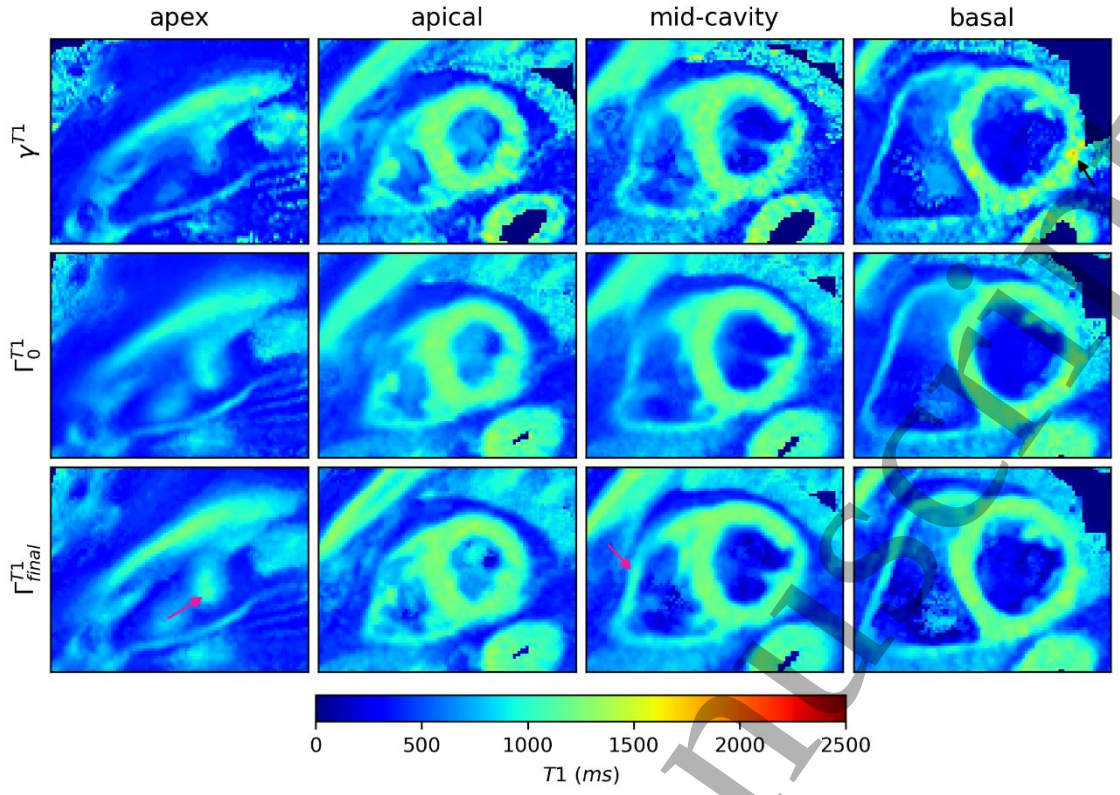

Figure 10: Four selected slices (apex, apical, mid-cavity and basal) before and after SRR. The visualization of the apex and the right ventricle improved in the SRR result $\Gamma_{\mathrm{final}}^{\mathrm{T1}}$ compared to its initialization Γ_0^{T1} and a single LR stack γ^{T1} (pink arrow in apex and mid-cavity slice). SRR reduced artefacts (black arrow in basal slice). All the results shown were obtained with the proposed moco approach.

In Figure 10, four selected slices (apex, apical, mid-cavity and basal) of γ^{T1}, Γ_0^{T1}, $\Gamma_{\mathrm{final}}^{\mathrm{T1}}$ are compared in-plane. The apex was more clearly visible in the apex slice after SRR. The visualization of the right ventricle also improved after SRR. In addition, the combination of multiple LR slices in the SRR also reduced artefacts (black arrow in Figure 10) and improved e.g. the quantification of the inferolateral segment of the basal slice. d in the right ventricle increased from 2.4 ± 1.35 in γ^{m}, to 3.2 ± 1.63 in Γ_0^{m} and 3.35 ±1.39 in $\Gamma_{\mathrm{final}}^{\mathrm{T1}}$, thus an increasement of d by 40% from γ^{m} to $\Gamma_{\mathrm{final}}^{\mathrm{T1}}$. The edge sharpness in the anterior apical segment was 0.26 ± 0.04 in γ^{m}, 0.21 ± 0.02 in Γ_0^{m} and 0.26 ± 0.04 in $\Gamma_{\mathrm{final}}^{\mathrm{T1}}$. The sharpness of the ventricle was lower in the SRR initialization than in the LR images, which could be attributed to the mixing of the partial volume effects in the individual LR images when combining them for the initialization. SRR was able to restore the original edge sharpness of the LR images. T1 maps of the three other volunteers can be seen in Supporting Information Figure S1.

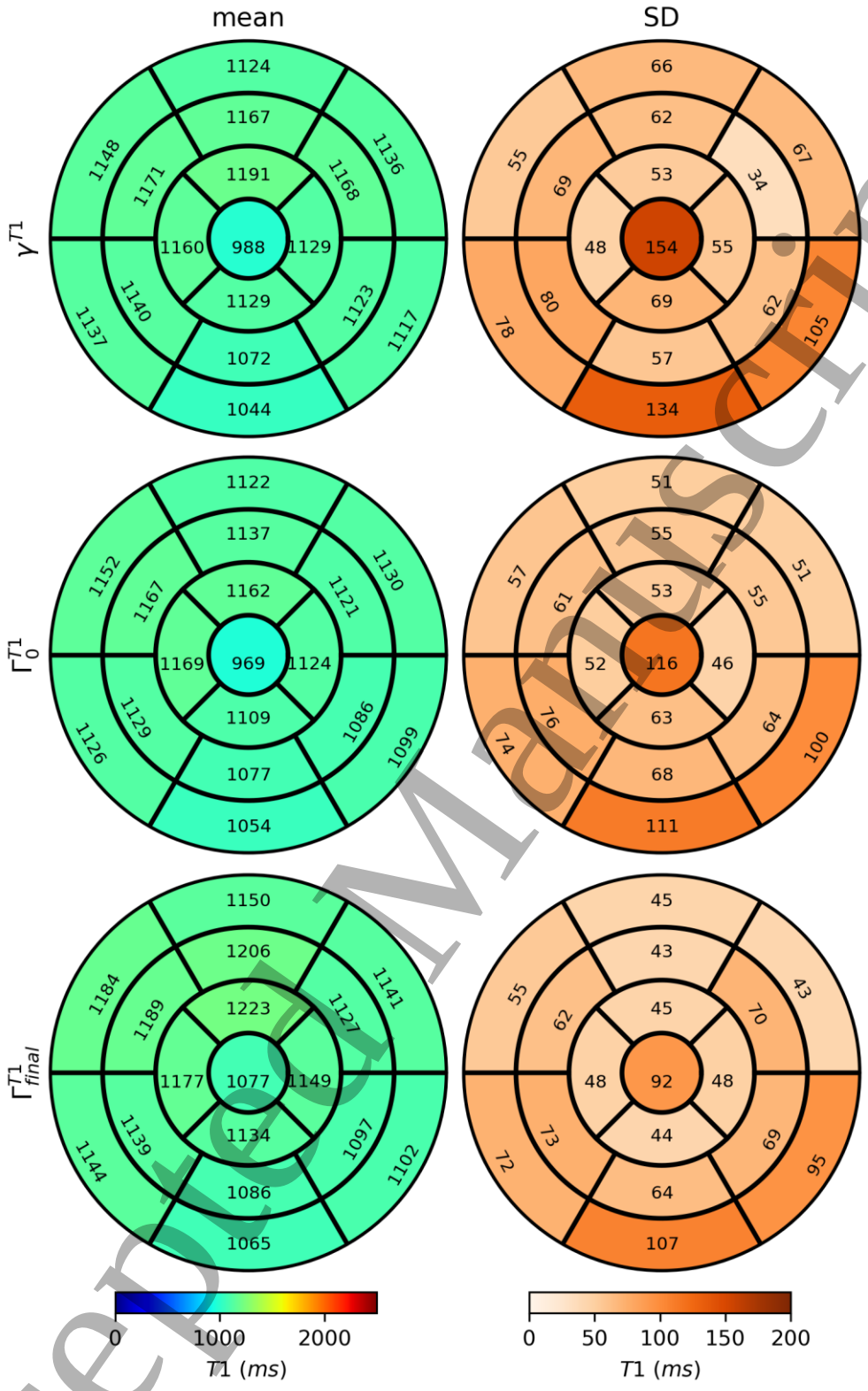

Figure 11: Bull's eye plots of the average T1 values in ms in standardized segments of the left ventricle and their standard deviation (SD). The SRR output Γ_{final}^{T1} is compared to a LR slice γ^{T1} and the SRR initialization Γ_0^{T1}.

Figure 11 shows the bulls-eye plots of γ^{T1}, Γ_0^{T1} and Γ_{final}^{T1}, averaged over four healthy volunteers. The SD before and after the SRR remained comparable, indicating that SRR did not affect the precision of the T1 values. The T1 values in the segments varied in Γ_{final}^{T1} by an average of 63.72 ms across the four healthy volunteers. The T1 intensities of the apex segment were underestimated before the SRR and showed a high SD. This was compensated by SRR.

Discussion

In this study, a novel motion-corrected model-based SRR approach was presented, providing 3D HR T1 maps in six to ten 17-seconds BH. The proposed model-based SRR scheme improved the visibility of small structures while the accuracy and precision of the T1 values after SRR remained comparably high. An alignment of different BH states showed great improvement of the SRR result.

Small structures, as e.g. the simulated fibrosis, the differentiation between phantom tubes and background or the right ventricle could be better visualized using SRR. Furthermore, anatomic information which was impaired in some LR stacks due to partial volume effects, as e.g. the apex, was successfully recovered by the proposed SRR approach.

An improvement in the imaging of small features by SRR can be concluded from the improved visualization of small structures in all volunteers of the in vivo experiments, such as in the right ventricle.

The accurate mapping of the right ventricular myocardium poses a great challenge due to its small thickness but would help to improve the diagnosis of e.g. right ventricular myocarditis or arrhythmogenic right ventricular cardiomyopathy. Its assessment could be improved by SRR, moving towards whole heart T1 mapping in the future.

The results were compared to a clinical reference scan and the T1 values after SRR were in good agreement with both the reference values resulting from the modified Look-Locker inversion recovery reference scan and those presented in literature[48]. The small underestimation of the myocardial T1 values after the SRR compared to reference values was probably due to the use of a slice-selective inversion pulse. A similar underestimation of the T1 values was reported in [49], which was attributed to magnetization transfer effects. A direct comparison of the SRR results to an in vivo reference scan was however difficult since this was acquired in another BH, hence showing a different motion state. Thus, the accuracy of the T1 values could only be determined in phantom measurement but not in the volunteer scans.

The proposed approach was not compared to previously published 3D T1 mapping frameworks as for example MR multitasking[50] or MR fingerprinting[51]. Nonetheless, the

publications in this field have either not resulted in isotropic voxel sizes[52–59] or a longer total scan time[6,7,60] compared to the proposed approach.

The precision of the T1 values was not calculated with a retest but as the SD over several healthy volunteers. It was assumed, that the T1 values of the myocardium were similar in all healthy volunteers.

One limitation of this approach is that T1 values of voxels representing blood could not be estimated and appeared shortened, due to the in-flow effect caused by the slice-selective inversion pulse. The slice-selective inversion pulse only inverted the blood spins that were in the corresponding slice at the time of the inversion. In the course of the cardiac cycle, these were replaced by inflowing, non-inverted blood spins, which then lead to an apparent shortening of the T1 value of the blood[43]. To still be able to calculate the extracellular volume, a further fast acquisition of a single LR slice with a global inversion pulse would provide the necessary information about the blood pool T1 values.

Every stack was acquired in a separate BH. Due to variations in BH, an alignment of different BH states was necessary before SRR. In agreement with [22], motion estimation was a key step in the SRR process and significantly affected the quality of the SRR result. Imperfectness in moco could lead to artefacts after SRR.

In clinical practice, 17 seconds BH are sometimes not feasible. To adapt the BH duration, the acquisition time per stack would need to be reduced and compensated for by acquiring more stacks in total. Due to the higher number of stacks, the proposed moco approach would have an even greater influence on the SRR result.

Compared to brain T1 mapping, cardiac imaging is restricted with respect to the number of LR slices per stack, due to limited BH time. To still cover a specific field-of-view in the slice encoding direction, gaps needed to be introduced between the LR slices. To compensate for these gaps, more stacks of LR slices needed to be acquired. According to [28], the more stacks used, the greater the degrading influence of inaccuracies in the motion registration on the SRR.

The stacks were planned such that they overlapped with each other by 1.5-2 mm. As each stack was obtained in a different BH position, the original distribution of stacks was impaired, even if the respiratory motion was correctly detected and estimated. Overall, the detectability of the simulated fibrosis was high in most of the motion corrected SRR maps. Nevertheless, depending on the distribution of stacks relative to each other after moco, the depiction of the fibrosis could still be impaired. This effect could in future be reduced by orientating the LR stacks differently (e.g. rotated to each other) along the slice encoding direction, which has also previously shown to improve SRR reconstructions compared to shifting the LR stacks[61].

The results of the moco could be improved by its integration into the optimization scheme of the SRR, as described in [62]. Furthermore, integrating rotation and deformation into the moco would probably further improve the alignment of BH states. Next to that, registering the slices within one stack separately to the HR volume would also account for inter stack motion due to poor breath holding. In addition, instead of retrospective BH correction, the position of the slices could be tracked prospectively and the acquisition adjusted accordingly, for example using the Pilot tone[63]. Next to that, SRR is not limited to T1 mapping, but could be extended to other quantitative parameters such as T2[64], for example using MR multitasking[50] or MR fingerprinting[51]. To improve the overall result of the SRR in future approaches, the SRR optimization scheme could be integrated in a model-based reconstruction framework as performed in [21]. By that, the SRR would incorporate the acquired raw data in the entire reconstruction optimization scheme instead of using it only in the model-based T1 reconstruction as in the presented approach.

This work was only evaluated in healthy volunteers, nevertheless, from the improved visualization of pathologies in the simulated data, it can be concluded that SRR might lead to an improved image quality in patients as well.

Conclusion

In this study, a novel motion-corrected cardiac model-based SRR approach was presented, providing 3D HR T1 maps in six to ten 17 seconds BH. The proposed approach was successfully applied in four healthy volunteers leading to improved visualization of small structures and precise T1 values. In future studies, an integration of the BH alignment and the T1 reconstruction into the optimization scheme could further improve the results.

Acknowledgment

The authors gratefully acknowledge funding from the German Research Foundation (GRK2260, BIOQIC).

The results presented here have been developed in the framework of the 18HLT05 QUIERO Project. This project has received funding from the EMPIR programme co-financed by the Participating States and from the European Union's Horizon 2020 research and innovation programme.

Ethical Statement

The research was approved by the institution's ethical committee ("Ethikkommission der PTB"). The research was conducted in accordance with the principles embodied in the Declaration of Helsinki and in accordance with local statutory requirements. All subjects gave written informed consent before participation. No approval ID number was specified.

References

1. Guo R, Weingärtner S, Šiurytė P, et al. Emerging Techniques in Cardiac Magnetic Resonance Imaging. *Journal of Magnetic Resonance Imaging*. 2022;55(4):1043-1059. doi:10.1002/jmri.27848

2. Haaf P, Garg P, Messroghli DR, Broadbent DA, Greenwood JP, Plein S. Cardiac T1 Mapping and Extracellular Volume (ECV) in clinical practice: a comprehensive review. *J Cardiovasc Magn Reson*. 2016;18(1):89. doi:10.1186/s12968-016-0308-4

3. Schelbert EB, Messroghli DR. State of the Art: Clinical Applications of Cardiac T1 Mapping. *Radiology*. 2016;278(3):658-676. doi:10.1148/radiol.2016141802

4. Al-Wakeel-Marquard N, Seidel F, Herbst C, et al. Diffuse myocardial fibrosis by T1 mapping is associated with heart failure in pediatric primary dilated cardiomyopathy. *Int J Cardiol*. 2021;333:219-225. doi:10.1016/j.ijcard.2021.03.023

5. Becker KM, Schulz-Menger J, Schaeffter T, Kolbitsch C. Simultaneous high-resolution cardiac T 1 mapping and cine imaging using model-based iterative image reconstruction. *Magn Reson Med*. 2019;81(2):1080-1091. doi:10.1002/mrm.27474

6. Qi H, Jaubert O, Bustin A, et al. Free-running 3D whole heart myocardial T 1 mapping with isotropic spatial resolution. *Magn Reson Med*. 2019;82(4):1331-1342. doi:10.1002/mrm.27811

7. Qi H, Bustin A, Kuestner T, et al. Respiratory motion-compensated high-resolution 3D whole-heart T1ρ mapping. *Journal of Cardiovascular Magnetic Resonance*. 2020;22(1):12. doi:10.1186/s12968-020-0597-5

8. Becker KM, Blaszczyk E, Funk S, et al. Fast myocardial T 1 mapping using cardiac motion correction. *Magn Reson Med*. 2020;83(2):438-451. doi:10.1002/mrm.27935

9. Plenge E, Poot DHJ, Bernsen M, et al. Super-resolution methods in MRI: Can they improve the trade-off between resolution, signal-to-noise ratio, and acquisition time? *Magn Reson Med*. 2012;68(6):1983-1993. doi:10.1002/mrm.24187

10. Greenspan H, Oz G, Kiryati N, Peled S. MRI inter-slice reconstruction using super-resolution. *Magn Reson Imaging*. 2002;20(5):437-446. doi:10.1016/S0730-725X(02)00511-8

11. de Senneville BD, Cardiet CR, Trotier AJ, et al. Optimizing 4D abdominal MRI: image denoising using an iterative back-projection approach. *Phys Med Biol*. 2020;65(1):015003. doi:10.1088/1361-6560/ab563e

12. Ebner M, Wang G, Li W, et al. An automated framework for localization, segmentation and super-resolution reconstruction of fetal brain MRI. *Neuroimage*. 2020;206(May 2019):116324. doi:10.1016/j.neuroimage.2019.116324

13. Gholipour A, Estroff JA, Warfield SK. Robust Super-Resolution Volume Reconstruction From Slice Acquisitions: Application to Fetal Brain MRI. *IEEE Trans Med Imaging*. 2010;29(10):1739-1758. doi:10.1109/TMI.2010.2051680

14. Kainz B, Steinberger M, Wein W, et al. Fast Volume Reconstruction From Motion Corrupted Stacks of 2D Slices. *IEEE Trans Med Imaging*. 2015;34(9):1901-1913. doi:10.1109/TMI.2015.2415453

15. Kuklisova-Murgasova M, Quaghebeur G, Rutherford MA, Hajnal J V., Schnabel JA. Reconstruction of fetal brain MRI with intensity matching and complete outlier removal. *Med Image Anal*. 2012;16(8):1550-1564. doi:10.1016/j.media.2012.07.004

16. McDonagh S, Hou B, Alansary A, et al. Context-Sensitive Super-Resolution for Fast Fetal Magnetic Resonance Imaging. In: *Lecture Notes in Computer Science (Including Subseries Lecture Notes in Artificial Intelligence and Lecture Notes in Bioinformatics)*. Vol 10555 LNCS. ; 2017:116-126. doi:10.1007/978-3-319-67564-0_12

17. Shuzhou Jiang, Hui Xue, Glover A, Rutherford M, Hajnal JV. A Novel Approach to Accurate 3D High Resolution and High SNR Fetal Brain Imaging. In: *3rd IEEE International Symposium on Biomedical Imaging: Macro to Nano, 2006.* Vol 2006. IEEE; 2006:662-665. doi:10.1109/ISBI.2006.1625003

18. Sui Y, Afacan O, Gholipour A, Warfield SK. Isotropic MRI Super-Resolution Reconstruction with Multi-scale Gradient Field Prior. In: Shen D, Liu T, Peters TM, et al., eds. *Physiology & Behavior*. Vol 11766. Lecture Notes in Computer Science. Springer International Publishing; 2019:3-11. doi:10.1007/978-3-030-32248-9_1

19. Sui Y, Afacan O, Gholipour A, Warfield SK. Fast and High-Resolution Neonatal Brain MRI Through Super-Resolution Reconstruction From Acquisitions With Variable Slice

Selection Direction. *Front Neurosci*. 2021;15(June):1-15. doi:10.3389/fnins.2021.636268

20. Van Steenkiste G, Poot DHJ, Jeurissen B, et al. Super-resolution T 1 estimation: Quantitative high resolution T 1 mapping from a set of low resolution T 1 -weighted images with different slice orientations. *Magn Reson Med*. 2017;77(5):1818-1830. doi:10.1002/mrm.26262

21. Bano W, Piredda GF, Davies M, et al. Model-based super-resolution reconstruction of T 2 maps. *Magn Reson Med*. 2020;83(3):906-919. doi:10.1002/mrm.27981

22. Van Reeth E, Tham IWK, Tan CH, Poh CL. Super-resolution in magnetic resonance imaging: A review. *Concepts in Magnetic Resonance Part A*. 2012;40A(6):306-325. doi:10.1002/cmr.a.21249

23. Basty N, Grau V. Super Resolution of Cardiac Cine MRI Sequences Using Deep Learning. In: *Lecture Notes in Computer Science (Including Subseries Lecture Notes in Artificial Intelligence and Lecture Notes in Bioinformatics)*. Vol 11040 LNCS. Springer International Publishing; 2018:23-31. doi:10.1007/978-3-030-00946-5_3

24. Bhatia KK, Price AN, Shi W, Hajnal J V, Rueckert D. Super-resolution reconstruction of cardiac MRI using coupled dictionary learning. In: *2014 IEEE 11th International Symposium on Biomedical Imaging (ISBI)*. IEEE; 2014:947-950. doi:10.1109/ISBI.2014.6868028

25. Corona V, Aviles-Rivero A, Debroux N, Le Guyader C, Schönlieb CB. Variational multi-task MRI reconstruction: Joint reconstruction, registration and super-resolution. *Med Image Anal*. 2021;68(August):101941. doi:10.1016/j.media.2020.101941

26. Dzyubachyk O, Tao Q, Poot DHJ, et al. Improved Myocardial Scar Characterization by Super-Resolution Reconstruction in Late Gadolinium Enhanced MRI. In: ; 2013:147-154. doi:10.1007/978-3-642-40760-4_19

27. Odille F, Bustin A, Chen B, Vuissoz PA, Felblinger J. Motion-Corrected, Super-Resolution Reconstruction for High-Resolution 3D Cardiac Cine MRI. In: *Lecture Notes in Computer Science (Including Subseries Lecture Notes in Artificial Intelligence and Lecture Notes in Bioinformatics)*. Vol 9351. ; 2015:435-442. doi:10.1007/978-3-319-24574-4_52

28. Rahman S ur, Wesarg S. Upsampling of cardiac MR images: Comparison of averaging and super-resolution for the combination of multiple views. In: *Proceedings of the 10th*

IEEE International Conference on Information Technology and Applications in Biomedicine. Vol 10. IEEE; 2010:1-4. doi:10.1109/ITAB.2010.5687693

29. Rahman S u., Wesarg S. Combining short-axis and long-axis cardiac MR images by applying a super-resolution reconstruction algorithm. In: Dawant BM, Haynor DR, eds. *Medical Imaging 2010: Image Processing*. Vol 7623. ; 2010:76230I. doi:10.1117/12.844356

30. Shi W, Caballero J, Ledig C, et al. Cardiac Image Super-Resolution with Global Correspondence Using Multi-Atlas PatchMatch. In: *Lecture Notes in Computer Science (Including Subseries Lecture Notes in Artificial Intelligence and Lecture Notes in Bioinformatics)*. Vol 8151. ; 2013:9-16. doi:10.1007/978-3-642-40760-4_2

31. Xia Y, Ravikumar N, Greenwood JP, Neubauer S, Petersen SE, Frangi AF. Super-Resolution of Cardiac MR Cine Imaging using Conditional GANs and Unsupervised Transfer Learning. *Med Image Anal*. 2021;71:102037. doi:10.1016/j.media.2021.102037

32. Beirinckx Q, Jeurissen B, Nicastro M, et al. Model-based super-resolution reconstruction with joint motion estimation for improved quantitative MRI parameter mapping. *Computerized Medical Imaging and Graphics*. Published online May 2022:102071. doi:10.1016/j.compmedimag.2022.102071

33. Beirinckx Q, Ramos-Llordén G, Jeurissen B, et al. Joint Maximum Likelihood Estimation of Motion and T1 Parameters from Magnetic Resonance Images in a Super-resolution Framework: a Simulation Study. Brunetti S, Dulio P, Frosini A, Rozenberg G, eds. *Fundam Inform*. 2020;172(2):105-128. doi:10.3233/FI-2020-1896

34. Block KT, Uecker M, Frahm J. Undersampled radial MRI with multiple coils. Iterative image reconstruction using a total variation constraint. *Magn Reson Med*. 2007;57(6):1086-1098. doi:10.1002/mrm.21236

35. Rueckert D, Sonoda LI, Hayes C, Hill DLG, Leach MO, Hawkes DJ. Nonrigid registration using free-form deformations: application to breast MR images. *IEEE Trans Med Imaging*. 1999;18(8):712-721. doi:10.1109/42.796284

36. Padfield D. Masked Object Registration in the Fourier Domain. *IEEE Transactions on Image Processing*. 2012;21(5):2706-2718. doi:10.1109/TIP.2011.2181402

37. Rund A, Aigner CS, Kunisch K, Stollberger R. Simultaneous multislice refocusing via time optimal control. *Magn Reson Med*. 2018;80(4):1416-1428. doi:10.1002/mrm.27124

38. Pauly J, Le Roux P, Nishimura D, Macovski A. Parameter relations for the Shinnar-Le Roux selective excitation pulse design algorithm (NMR imaging). *IEEE Trans Med Imaging*. 1991;10(1):53-65. doi:10.1109/42.75611

39. Wang Y, Yang J, Yin W, Zhang Y. A New Alternating Minimization Algorithm for Total Variation Image Reconstruction. *SIAM J Imaging Sci*. 2008;1(3):248-272. doi:10.1137/080724265

40. Chambolle A. An Algorithm for Total Variation Minimization and Applications. *J Math Imaging Vis*. 2004;20(1/2):89–97. doi:10.1023/B:JMIV.0000011325.36760.1e

41. Liu DC, Nocedal J. On the limited memory BFGS method for large scale optimization. *Math Program*. 1989;45(1-3):503-528. doi:10.1007/BF01589116

42. Segars WP, Sturgeon G, Mendonca S, Grimes J, Tsui BMW. 4D XCAT phantom for multimodality imaging research. *Med Phys*. 2010;37(9):4902-4915. doi:10.1118/1.3480985

43. Keith GA, Rodgers CT, Chappell MA, Robson MD. A look-locker acquisition scheme for quantitative myocardial perfusion imaging with FAIR arterial spin labeling in humans at 3 tesla. *Magn Reson Med*. 2017;78(2):541-549. doi:10.1002/mrm.26388

44. Scott AD, Keegan J, Firmin DN. Motion in Cardiovascular MR Imaging. *Radiology*. 2009;250(2):331-351. doi:10.1148/radiol.2502071998

45. Captur G, Gatehouse P, Keenan KE, et al. A medical device-grade T1 and ECV phantom for global T1 mapping quality assurance — the T 1 Mapping and ECV Standardization in cardiovascular magnetic resonance (T1MES) program. *Journal of Cardiovascular Magnetic Resonance*. Published online 2016:1-20. doi:10.1186/s12968-016-0280-z

46. Cerqueira MD, Weissman NJ, Dilsizian V, et al. Standardized Myocardial Segmentation and Nomenclature for Tomographic Imaging of the Heart. *Circulation*. 2002;105(4):539-542. doi:10.1161/hc0402.102975

47. Etienne A, Botnar RM, van Muiswinkel AMC, Boesiger P, Manning WJ, Stuber M. ?Soap-Bubble? visualization and quantitative analysis of 3D coronary magnetic resonance angiograms. *Magn Reson Med*. 2002;48(4):658-666. doi:10.1002/mrm.10253

48. von Knobelsdorff-Brenkenhoff F, Prothmann M, Dieringer MA, et al. Myocardial T1 and T2 mapping at 3 T: reference values, influencing factors and implications. *Journal of Cardiovascular Magnetic Resonance*. 2013;15(1):53. doi:10.1186/1532-429X-15-53

49. Huang L, Neji R, Nazir MS, et al. FASt single-breathhold 2D multislice myocardial T 1 mapping (FAST1) at 1.5T for full left ventricular coverage in three breathholds. *Journal of Magnetic Resonance Imaging*. 2020;51(2):492-504. doi:10.1002/jmri.26869

50. Christodoulou AG, Shaw JL, Nguyen C, et al. Magnetic resonance multitasking for motion-resolved quantitative cardiovascular imaging. *Nat Biomed Eng*. 2018;2(4):215-226. doi:10.1038/s41551-018-0217-y

51. Ma D, Gulani V, Seiberlich N, et al. Magnetic resonance fingerprinting. *Nature*. 2013;495(7440):187-192. doi:10.1038/nature11971

52. Velasco C, Cruz G, Lavin B, et al. Simultaneous T 1 , T 2 , and T 1ρ cardiac magnetic resonance fingerprinting for contrast agent–free myocardial tissue characterization. *Magn Reson Med*. 2022;87(4):1992-2002. doi:10.1002/mrm.29091

53. Nordio G, Henningsson M, Chiribiri A, Villa ADM, Schneider T, Botnar RM. 3D myocardial T 1 mapping using saturation recovery. *Journal of Magnetic Resonance Imaging*. 2017;46(1):218-227. doi:10.1002/jmri.25575

54. Nordio G, Bustin A, Odille F, et al. Faster 3D saturation-recovery based myocardial T1 mapping using a reduced number of saturation points and denoising. *PLoS One*. 2020;15(4). doi:10.1371/journal.pone.0221071

55. Mao X, Lee HL, Hu Z, et al. Simultaneous Multi-Slice Cardiac MR Multitasking for Motion-Resolved, Non-ECG, Free-Breathing T1–T2 Mapping. *Front Cardiovasc Med*. 2022;9(March):1-13. doi:10.3389/fcvm.2022.833257

56. Han PK, Marin T, Djebra Y, et al. Free-breathing 3D cardiac T 1 mapping with transmit B 1 correction at 3T. *Magn Reson Med*. 2022;87(4):1832-1845. doi:10.1002/mrm.29097

57. Guo R, Chen Z, Wang Y, Herzka DA, Luo J, Ding H. Three-dimensional free breathing whole heart cardiovascular magnetic resonance T1 mapping at 3 T. *Journal of Cardiovascular Magnetic Resonance*. 2018;20(1):64. doi:10.1186/s12968-018-0487-2

58. Ferreira da Silva T, Galan-Arriola C, Montesinos P, et al. Single breath-hold saturation recovery 3D cardiac T1 mapping via compressed SENSE at 3T. *Magnetic Resonance*

Materials in Physics, Biology and Medicine. 2020;33(6):865-876. doi:10.1007/s10334-020-00848-2

59. Cruz G, Jaubert O, Qi H, et al. 3D free-breathing cardiac magnetic resonance fingerprinting. *NMR Biomed*. 2020;33(10):1-16. doi:10.1002/nbm.4370

60. Milotta G, Bustin A, Jaubert O, Neji R, Prieto C, Botnar RM. 3D whole-heart isotropic-resolution motion-compensated joint T 1 /T 2 mapping and water/fat imaging. *Magn Reson Med*. 2020;84(6):3009-3026. doi:10.1002/mrm.28330

61. Shilling RZ, Robbie TQ, Bailloeul T, Mewes K, Mersereau RM, Brummer ME. A Super-Resolution Framework for 3-D High-Resolution and High-Contrast Imaging Using 2-D Multislice MRI. *IEEE Trans Med Imaging*. 2009;28(5):633-644. doi:10.1109/TMI.2008.2007348

62. Dzyubachyk O, Tao Q, Poot DHJ, et al. Super-resolution reconstruction of late gadolinium-enhanced MRI for improved myocardial scar assessment. *Journal of Magnetic Resonance Imaging*. 2015;42(1):160-167. doi:10.1002/jmri.24759

63. Ludwig J, Speier P, Seifert F, Schaeffter T, Kolbitsch C. Pilot tone–based motion correction for prospective respiratory compensated cardiac cine MRI. *Magn Reson Med*. 2021;85(5):2403-2416. doi:10.1002/mrm.28580

64. Giri S, Chung YC, Merchant A, et al. T2 quantification for improved detection of myocardial edema. *Journal of Cardiovascular Magnetic Resonance*. 2009;11(1):56. doi:10.1186/1532-429X-11-56